Journal of the European Ceramic Society 16 (1996) 85–97

0955-2219(95)00118-2
0955-2219/96/$15.00

In-Plane Microstructure of Plasma-Sprayed Mg–Al Spinel and 2/1-Mullite Based Protective Coatings: An Electron Microscopy Study

W. Braue,[a] G. Paul,[a] R. Pleger,[a] H. Schneider[a] & J. Decker[b]

[a]German Aerospace Research Establishment (DLR), Materials Research Institute, D-51147 Cologne, Germany
[b]German Institute for Refractories and Ceramics, D-53113 Bonn, Germany

(Received 30 January 1995; revised version received 12 June 1995; accepted 23 June 1995)

Abstract

Planar specimens prepared from thin plasma-sprayed Mg–Al spinel and 2/1-mullite layers are investigated via conventional and analytical transmission electron microscopy in order to evaluate the constraints of rapid solidification on the in-plane microstructure at different scales of resolution.

Despite intrinsic differences in the nature and density of structural defects between the two materials studied, their gross-scale microstructures share a characteristic sequence starting from (i) large, spherical core grains, followed by (ii) a radial chill-zone exhibiting columnar to dendritic grain morphologies, which eventually leads to (iii) an impingement zone formed by the intersection of different chill-zones.

Relief of thermomechanical strain from the core grains and chill zones gives rise to an equiaxed subgrain architecture and intensive microcracking in the impingement zone. Moreover, the impingement zone represents the region of highest and most varied lattice defect density.

1 Introduction

Plasma-sprayed oxide coatings deposited on metallic or ceramic substrates define a unique class of materials which are well established in different fields of industrial application, such as thermal insulation (thermal barrier coatings), protection against oxidation or corrosive attack, and wear resistance.

Coating materials particularly pursued in this approach are zirconia,[1–3] alumina,[4–7] cordierite $Mg_2Al_3[AlSi_5O_{18}]$[8] and forsterite Mg_2SiO_4.[8] Because of their good thermal shock resistance, spinel ($MgAl_2O_4$) coatings have been exploited for various applications in chemical engineering and steel production.[9,10] Mullite, $Al_{4+x}Si_{2-2x}O_{10-x}$ (with $0{\cdot}2 < x < 0{\cdot}5$) exhibits an oxygen-deficient orthorhombic structure, where x defines the number of oxygen atoms missing per unit cell.[11–13] This constituent is a potential candidate for thermal protection layers since it offers high thermal stability and good thermal shock resistance along with both low thermal expansion and low thermal conductivity.[14,15] Because of the close match in thermal expansion coefficients, mullite-based protective layers also perform well as corrosion resistant coatings for SiC-based heat exchanger tubes.[16] Moreover, mullite has been successfully employed as an oxidation-resistant coating for molybdenum substrates.[17,18]

Besides their attractive thermomechanical properties, a major motivation for selection of spinel and mullite plasma-deposited layers in the present research stems from the fact that both materials are ideally suited as model components in extended alumina systems. Alumina is certainly one of the best studied ceramic plasma-sprayed systems in the literature (see Ref. 7 for review). It is a principal constituent in the SiO_2–Al_2O_3[19] and MgO–Al_2O_3[20] phase diagrams. Alumina polymorphs were reported to occur in spinel and mullite microstructures in case of deviations from stoichiometry and/or kinetic constraints during cool-down.[21–23]

Non-equilibrium conditions during ultrasonic transport and deposition of plasma-sprayed materials create a complex pattern of interdependent experimental parameters. Because of the extreme quenching rates during deposition, which are of the order of 10^6 K s^{-1},[8,9] the microstructures and thus the physical properties of plasma-sprayed materials differ significantly from their conventionally densified counterparts.[24–27]

The present study focuses on the lateral microstructural variation during the first stage of

coating build-up. Plane view transmission electron microscopy (TEM) specimens were prepared from thin layers of thermally sprayed Mg–Al spinel and 2/1-mullite and investigated by means of conventional and analytical TEM. The so-derived 2D microstructural features are referred to as in-plane microstructure. This approach particularly addresses the following aspects:

(i) the gross microstructure (grain size, grain morphology, macroporosity) of as-sprayed deposits on a micron scale;
(ii) the phase stability during plasma-spraying, focusing on the occurrence of metastable phases due to local variations in the cooling rate during deposition; and
(iii) the nature and density of structural defects in the as-sprayed grains, which are expected due to varying high stresses during impact with the cold substrate.

The two-dimensional microstructural analysis of a thin protective coating as pursued in this study is a simplified approach which has its limitations in assessing variations of grain morphology and texture normal to the substrate surface. The interaction of newly arrived with previously deposited material during solidification depends on the heat flux gradient[1,7] through the layer in a complex manner, thus turning the thickening process of the coating into more than just a simple 3D layer by layer repetition of the in-plane microstructure. For most applications however, the very first layers of the as-sprayed microstructure are crucial for the performance of the coating, particularly in terms for adhesion between the substrate and the protective coating. Moreover, a well-defined reference plane is mandatory for addressing the complex microstructure of layered structures such as plasma-sprayed materials. Therefore, it is anticipated that an assessment of the in-plane microstructural features including different scales of resolution (macroscopic versus microscopic) will contribute valuable information for further optimization of plasma-sprayed thermal protection layers and a better understanding of the 3D architecture within thick coatings.

2 Experimental Procedures

Mullite powder derived from melt-grown ('fused-mullite') batches exhibiting a powder particle size distribution of 10–40 μm was supplied by Huels Inc., Troisdorf, Germany. The spinel powder derived from melt-grown material (grain size between 20 and 40 μm) was obtained from the same supplier.

A Metco 4 MP plasma gun utilizing a gun power of 375 kW was employed in this study using N_2 as primary gas (flow rate 35 l min^{-1}), H_2 as secondary gas (flow rate 7 l min^{-1}) and N_2 as carrier gas, respectively. The powders were sprayed from a distance of 70 mm on to the surface of a sillimanite (Al_2SiO_5) substrate utilizing an average feeding rate of 40 g min^{-1}. The substrate was not preheated, resulting in relatively poor adhesion of the coatings and predominantly lateral heat flow through the coating. The average thickness of the plasma-sprayed layers after several passes was of the order of 100 μm.

A Philips EM 430T TEM/STEM transmission electron microscope operating at 300 kV was employed in this study. The very first layer of the coatings adjacent to the substrate were sampled for preparation of plane view specimens. Electron-transparent thin foils were prepared by standard ceramographic techniques involving dimpling and 5 keV argon ion-beam thinning. HREM images (see Section 3.3) were processed by a digital image processing system consisting of a CCD-camera, a frame-grabber, a personal computer and an image processing program (Synoptics Ltd, UK).

3 Results and Discussion

The gross-scale microstructural patterns of as-sprayed spinel and mullite coatings are described in Section 3.1. In the two subsequent sections we first comment on intrinsic characteristics of the spinel and the mullite microstructure, such as the phase stability during transport and deposition (Section 3.2), and then discuss the defect structure of as-sprayed grains (Section 3.3).

3.1 General microstructure of as-sprayed spinel and mullite layers

Solidification of as-sprayed ceramic coatings is primarily controlled by local heat flux gradients utilizing free surfaces for heterogeneous nucleation, such as the periphery of large grains. This issue has been emphasized in previous research[7] for both as-sprayed metallic alloys and Al_2O_3-rich ceramics and we also found it to be an important concept for both plasma-sprayed materials investigated in this study.

The occurrence of large spherical grains embedded in a fine-grained matrix of different grain morphology defined a characteristic microstructural feature for both spinel and mullite layers. The large grains defined the nucleation 'core' (following a notation employed in Ref. 7 for as-sprayed metallic coatings) of a characteristic sequence of the in-plane microstructure. This pattern can be rationalized in terms of a three-step

development (stages I–III), which also comprises the chronology during deposition and solidification. The core grains are referred as stage I. Figure 1 gives a typical example for a core grain in the spinel layer imaged at low magnification. Because core grains generally were homogeneous single-phase with a grain size about the same as the particle size of the starting batch, they probably represent primary constituents which were only marginally melted in the plasma torch and resolidified on the substrate without being fragmentated during impact. It is important to note that with the exception of occasional twinning in the mullite system (see Section 3.2), a very low-defect density was-observed in all the core grains examined.

Due to the relatively poor adhesion of the as-sprayed materials to the sillimanite substrate, the preferred direction of the heat flow during cool-down is supposed to extend within the plasma layers rather than normal towards the substrate. The radial temperature gradient extending perpendicular to the surface of the core grains in the plane of the coating favoured the development of defect-free columnar grains with their growth axes parallel to the direction of the heat flux. Because this growth morphology is very similar to the chill-zone observed in solidified ingots,[28] this microstructure is referred as the 'chill-zone' or region II. This zone of columnar grain growth (labelled region 2 in Figs 1 and 2) extends radially from the large core grains until it eventually interferes with similar chill-zones from other core grains to create an 'impingement zone' (region 3 in Fig. 1).

During the development of the in-plane microstructure the impingement zone is considered to

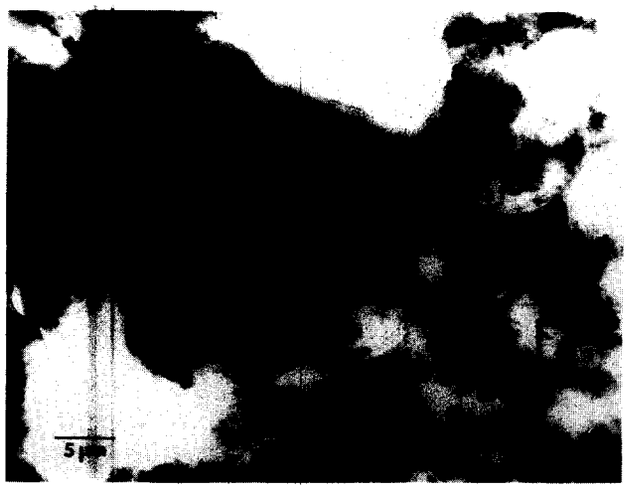

Fig. 1. TEM bright-field (BF) micrograph displaying the characteristic gross microstructure of an in-plane section of as-sprayed Mg–Al spinel layer: a large spherical core grain (region 1), followed by a chill-zone with columnar grain morphology (region 2), which eventually leads to an impingement zone (region 3) with intensive microcracking. Details of regions II and III are revealed in Figs 2 and 3, respectively.

Fig. 2. Chill-zone in spinel (region 2 in Fig. 1), exhibiting a typical columnar grain morphology around the periphery of a spinel core grain (TEM BF). The beam directions are parallel to [1 1 1] (core grain) and [0 1 $\bar{1}$] (chill-zone), respectively.

Fig. 3. Impingement zone in spinel (region 3 from Fig. 1), revealing mosaic-like microstructure (beam direction parallel [0 1 0]) and microcracks emerging from intersection of different chill-zones.

evolve last. In spinel (Fig. 3), it is characterized by a mosaic-like microstructure exhibiting an equiaxed subgrain morphology bounded by {1 0 0} and {1 1 0} planes, along with intensive microcracking and considerable intergranular porosity. As discussed in Section 3.3 in more detail, the impingement zone represents the region of highest lattice defect density. The noticeable change in grain morphology from columnar in the chill-zones to equiaxed in the impingement zone is attributed to a slowing of the cooling rate as the coating coverage of the substrate increases. This effect will favour more isotropic grain morphologies similar to observations of other plasma-sprayed materials.[1,7] It is assumed that the core grains represent the larger particle size fraction of the starting powder batch which were only partially molten during ultrasonic transport. In contrast, the microstructures of the chill- and impingement zones are considered to result from smaller, fully molten particle deposition on the substrate. After the quench from the liquid, solidification is controlled by anisotropic thermal gradients defined by the cooling conditions in the predeposited material.

The three-stage microstructural sequence [core grain (I) → chill-zone (II) → impingement zone (III)] was also observed for the mullite deposit, as summarized in Figs 4–7. The occurrence of columnar grains (Fig. 4) attached to the surface of large

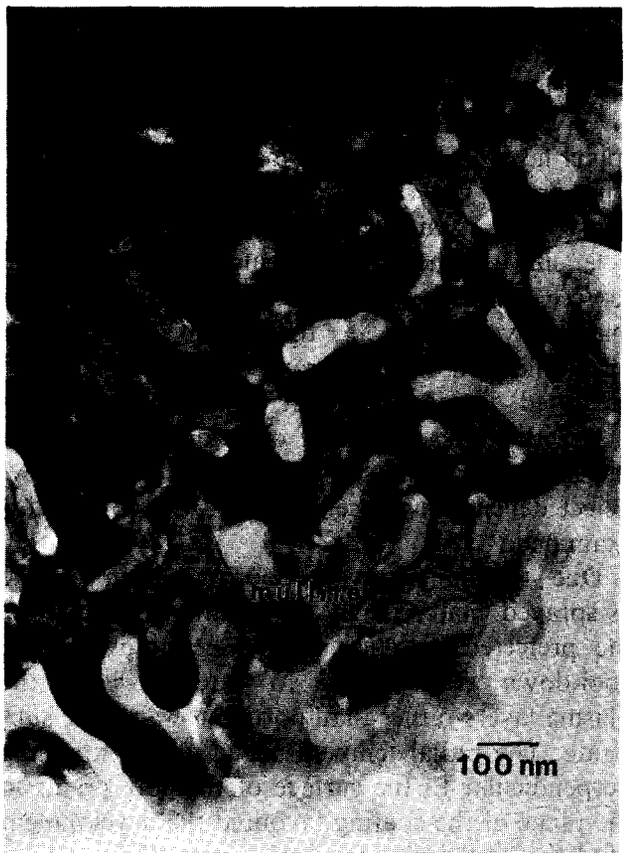

Fig. 5. Early stages in development of dendritic grain morphology in the mullite layer. Note the high density of intragranular porosity.

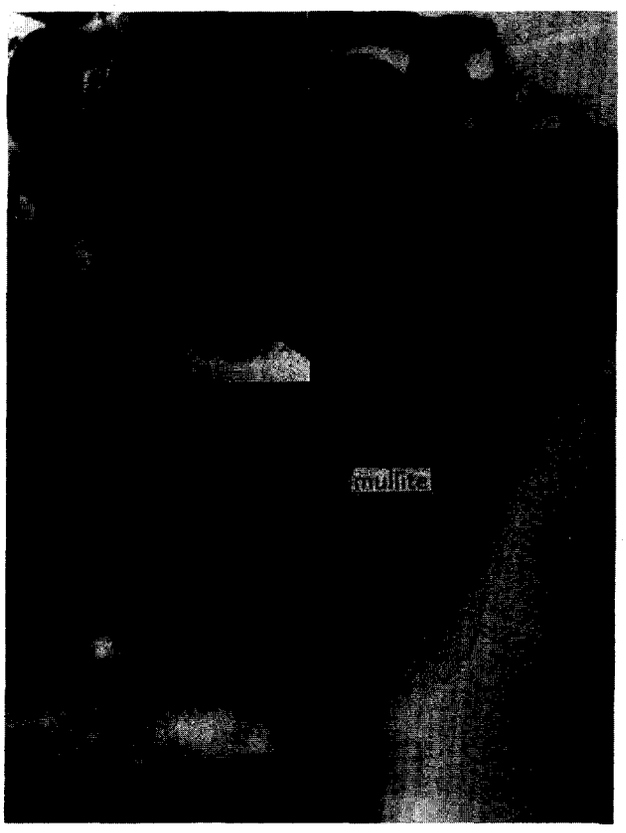

Fig. 4. Columnar grain morphology of as-sprayed mullite from chill-zone (labelled 2) close to core grain (labelled 1), as shown in the inset. Mullite orientation is parallel to [0 0 1].

Fig. 6. Final stage in development of dendritic grain morphology in as-sprayed mullite, embedded in amorphous phase (labelled g).

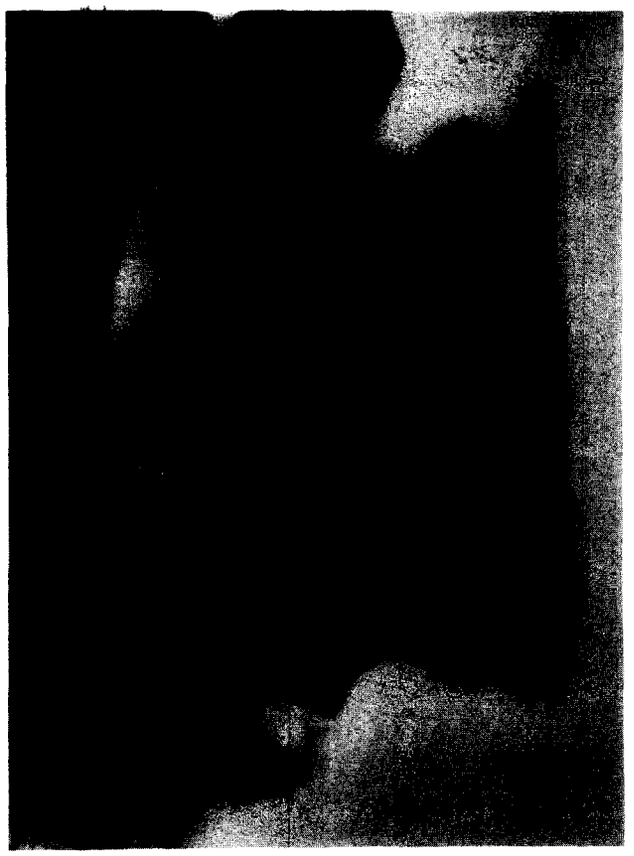

Fig. 7. Mullite aggregate attached to a continuous alumina- and silica-rich glassy phase (labelled g). Beam direction is parallel to [0 1 0].

core grains in the mullite layer indicates that its microstructural development was similar to spinel. The growth axis is approximately parallel to [1 1 0], deviating from the normal growth axis of mullite, which is parallel to [0 0 1].[29]

Locally the mullite grain morphology along the spreading chill-zone can change from columnar, through smooth droplet-like grains with isolated pockets of amorphous phase (Fig. 5) to, eventually, typical dendrites attached to a continuous interdendritic amorphous phase (Fig. 6), which is similar to the amorphous interlayer found in sintered bodies. The dendrite tips consist of macroscopic {1 1 0} planes, and the growth direction in this case is approximately parallel to [0 1 0]. Residual pockets of SiO_2-rich amorphous phase acting as a sink for Al and some impurities are associated with equiaxed mullite aggregates bound by {1 1 0} planes, as shown in Fig. 7. Such areas most likely represent local compositional deviations from the bulk, pushing the composition into the mullite plus SiO_2 field of the Al_2O_3–SiO_2 phase diagram.[19] Similar microstructures have been reported from directional solidification experiments in the Al_2O_3–SiO_2 system.[30] Compared to spinel, the mullite system seems to be particularly sensitive to fluctuations along the liquid/solid interface, which may be attributed to its lower intrinsic thermal conductivity and/or local variation in temperature gradient.

Impingement zones as defined by the intersection of chill-zones from several core grains are also established in the mullite deposits (see Fig. 8; to be compared with Fig. 3). The subgrain boundary network is often parallel to {1 1 0} planes. The dislocation density within the subgrains is low (see Section 3.3); most dislocations were single and isolated, but a few dipoles were observed.

In the spinel and mullite layers investigated, macroporosity is scattered heterogeneously throughout the in-plane microstructure (Fig. 9). Porosity is generally more pronounced in the mullite deposits. The pore size may reach a micron, with the pores bounded intragranularly in most cases. The pores are spherical, indicating entrapment of gaseous species in the molten, low-viscosity feedstock material during plasma spraying. An interlaminar type of macroporosity is also observed which gives rise to a characteristic striation pattern (Fig. 10) in the columnar grain structure of the chill-zone. On a much smaller scale compared to these macropores, the columnar mullite grains themselves exhibited numerous faceted intragranular pores (denoted by arrowheads in Fig. 10), very similar to Kirkendal voids in conventionally densified Al_2O_3-rich materials.[31,32]

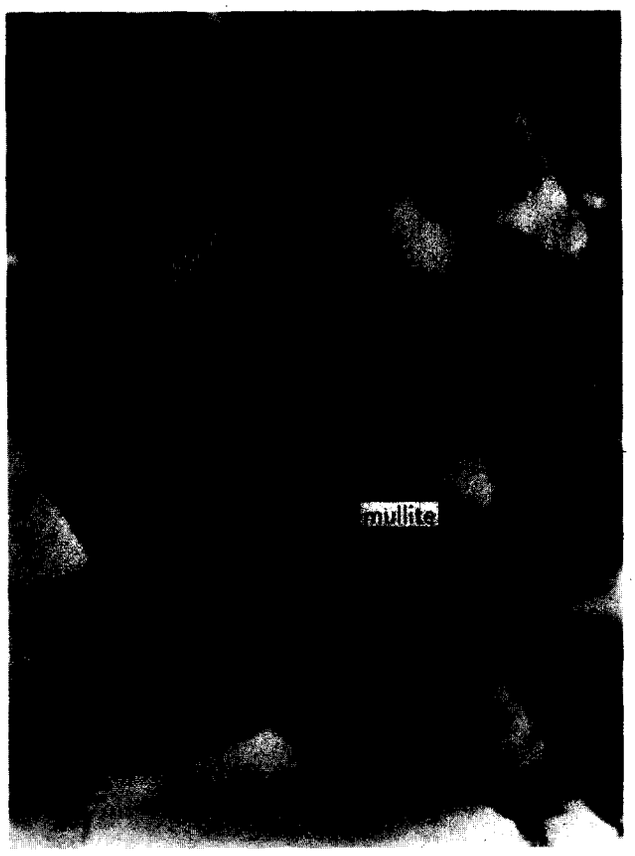

Fig. 8. Impingement zone in as-sprayed mullite (compare with Fig. 3). Small-angle grain boundaries and a rectangular {1 1 0} grain morphology create a mosaic-like pattern. Note the lack of intergranular porosity.

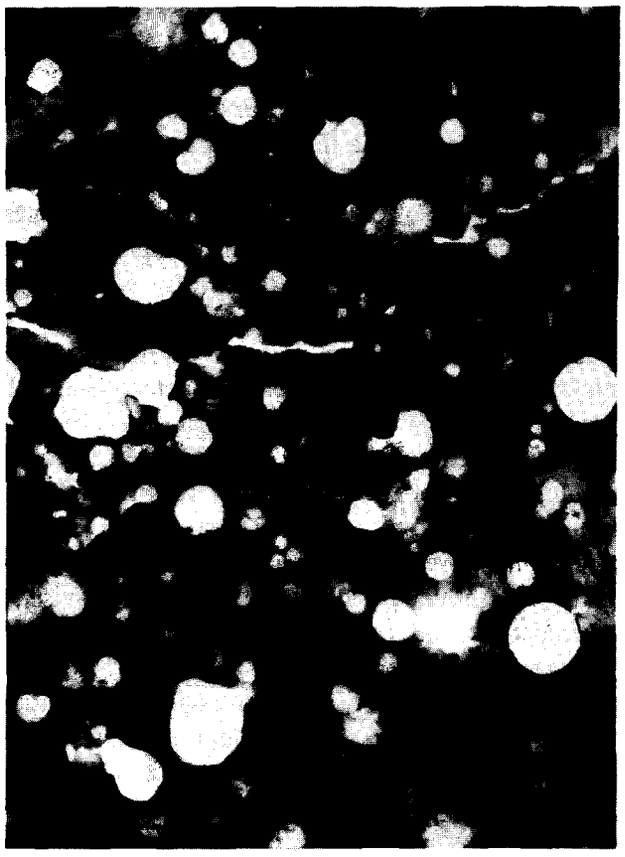

Fig. 9. Mullite layer exhibiting large-scale porosity, taken from area where the chill-zone meets the impingement zone.

Fig. 10. Columnar mullite grains exhibiting extensive interlaminar porosity (extending from top to bottom of micrograph) along with numerous faceted intragranular pores (indicated by arrows).

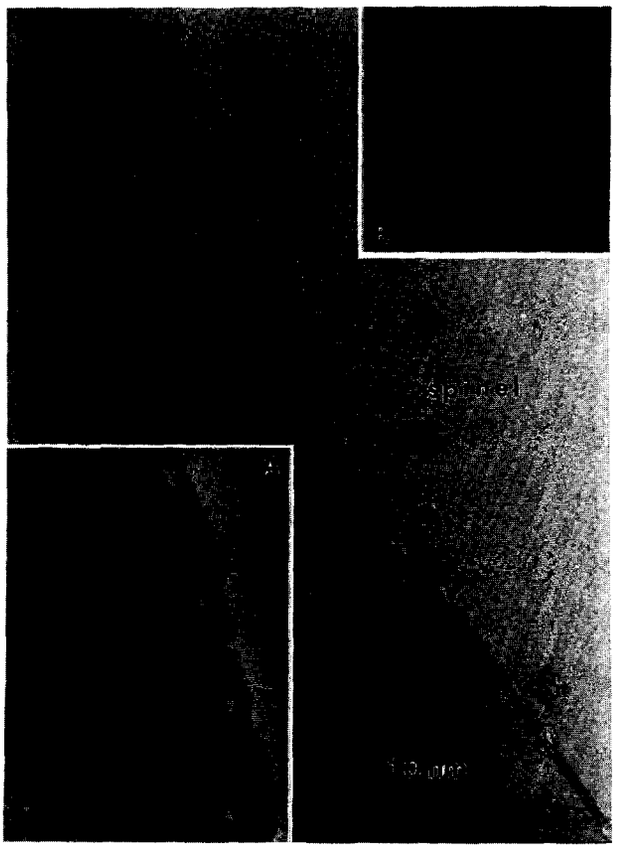

Fig. 11. Defocused BF image of edge-on grain boundary in spinel, revealing grain boundary precipitates. Inset A shows the wedge of a similar but tilted grain boundary, proving that the precipitates are strictly confined to the grain boundary. Inset B reveals a faceted amorphous precipitate bounded by low-energy spinel planes.

In contrast to the micropores concentrated in the mullite chill-zones, the spinel layers exhibited numerous submicrometre-sized features which are strictly confined to grain boundaries (Fig. 11). They are particularly abundant in the impingement zone where they coexist with the dislocations in the subgrain boundaries. In Fig. 11, a spinel grain boundary from a very thin region of the specimen is imaged edge-on under defocus conditions, revealing a sequence of tiny elongated 'precipitates' of the order of 10 nm. Inset A shows their accumulation within the wedge of a tilted grain boundary. These precipitates are (i) sometimes faceted (see inset B in Fig. 11) and (ii) consist of amorphous material, as revealed by convergent beam electron diffraction (CBED). During small-probe analysis in the microscope radiation effects occurred easily, so their composition was impossible to identify unambiguously.

The different types of macro- and microporosity affect both the elastic modulus and the thermal conductivity of the spinel and mullite layers. As an increased pore volume accounts for better relaxation of thermal stresses, as-sprayed ceramic materials exhibit superior thermal shock resis-

tance, compared to their dense counterparts.[24–27] Studies of plasma-sprayed PSZ-based thermal barrier coatings[2] have demonstrated that porosity is indeed a desirable microstructural parameter for those applications where harsh thermal cycling conditions, e.g. in engine components, define the major challenge for the performance of the protective coating. In conjunction with the anisotropic grain morphology of the in-plane microstructure, porosity and microcracks contribute to the non-elastic stress/strain behaviour reported for plasma-sprayed coatings.[26,27]

3.2 Phase stability and chemical gradients in as-sprayed spinel and mullite coatings

Phase stability in plasma-sprayed materials depends on kinetic and energetic constraints related to nucleation and growth of the constituents along the solid/liquid interface during quenching. These constraints control whether the chemical composition and constitution of the feedstock materials match that of the deposited layer. In this context plasma-sprayed alumina is a well-documented model system for the occurrence of metastable transition alumina phases due to rapid cool-down (see Ref. 7 for review).

As-sprayed spinel is a homogeneous single-phase material as demonstrated by small-probe microanalysis and electron diffraction. A large-angle CBED pattern demonstrated the characteristic three-fold symmetry along the [1 1 1] axis and corresponding HOLZ-line pattern in the (0 0 0) diffraction disc in agreement with the $MgAl_2O_4$ cell dimensions (Fig. 12). No γ-Al_2O_3 precipitates were detected in the spinel. These would be expected if substantial evaporation of MgO occurred causing formation of non-stoichiometric $(Al_2O_3)_nMgO$ ($n > 1$) spinels.[15]

Compared to the rather straightforward phase relationships in the binary MgO–Al_2O_3,[19,20] the Al_2O_3–SiO_2 system is more complex; metastable phase equilibria may arise due to notably slow nucleation kinetics for formation of mullite solid solutions and/or alumina during crystallization from a melt.[34,35] As discussed below in more detail, the basic mechanisms to accommodate chemical gradients during plasma spraying in the binary Al_2O_3–SiO_2 system is the formation of metastable transition alumina polymorphs, which are quite frequently observed. (The occasional formation of a mullite species which is more Al-rich and heavily twinned compared to the standard as-sprayed 2/1-mullite is most likely to be controlled by the stoichiometry of the mullite feedstock material (see Section 3.3).)

In as-sprayed mullite layers, single grains of cubic η-Al_2O_3 located at triple-grain junctions

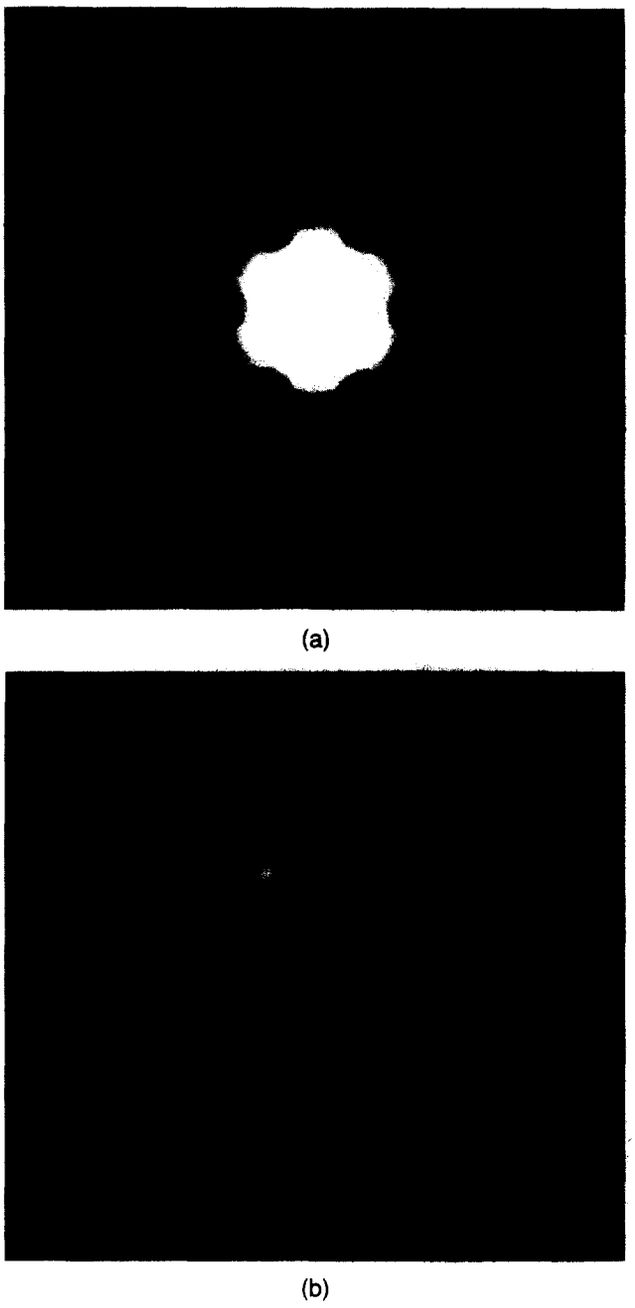

Fig. 12. CBED patterns obtained from spinel [1 1 1] core grain as displayed in Fig. 1. (a) Composite pattern consisting of zero-order Laue zone (ZOLZ) pattern plus first-order Laue zone (FOLZ) ring. (b) arrangement of the higher-order Laue zone (HOLZ) lines around the [1 1 1] pole in the central (0 0 0) disc clearly reveals a three-fold pattern, thus confirming the cubic symmetry of the crystal investigated.

were identified by selected area diffraction (Fig. 13). The zone axis of the selected area diffraction (SAD) pattern (see inset) is parallel to [1 1 $\bar{2}$] with continuous streaking along the <1 1 1> and <1 3 1> directions. The streaking is due to structural disorder of η-Al_2O_3 which has a spinel-type structure.[35–37] Often types of submicrometre-size intragranular inclusions were observed in the equiaxed subgrains from mullite impingement zones. A large secondary phase grain (Fig. 14(a)) located on a small-angle grain boundary was identified as monoclinic θ-Al_2O_3 by means of CBED (see insets A and B in

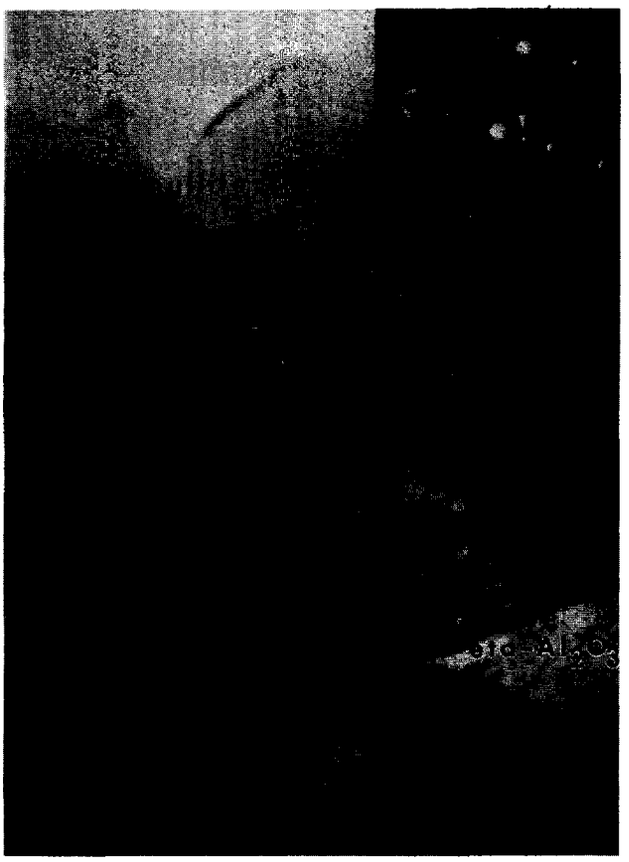

Fig. 13. n-Al_2O_3 at triple grain junction of as-sprayed 2/1-mullite. Orientation is parallel [1 1 $\bar{2}$]. Note streaking parallel to {1 1 1} and {1 3 1} in the SAD pattern inserted. Centre of SAD aperture is given by circle.

Fig. 14(b)). Tiny secondary phase inclusions with planar defects detected in the same area (Fig. 14(b)) were identified as transition alumina phases via digital image analysis.

The rationale for the formation of transition alumina polymorphs in as-sprayed layers instead of the thermodynamically stable phase corundum is based on the cooling rate and nucleation kinetics during plasma spraying:

(1) Plasma-sprayed alumina-rich ceramic systems have shown that the formation of metastable transition aluminas is mostly controlled by the cooling rate.[7] A slow cooling rate favours positioning of Al^{3+} in octahedral coordination, thus leading to the formation of corundum. Slow cooling is seldom achieved during plasma spraying. Instead, fast cooling rates which favour tetrahedral coordination of Al^{3+} are more common, which give rise to the formation of transition aluminas.

(2) The interaction of phase stability and cooling rate is clearly a function of the particle size.[7] Small particles are characterized by high quenching rates, favouring the formation of transition aluminas for reasons discussed previously.

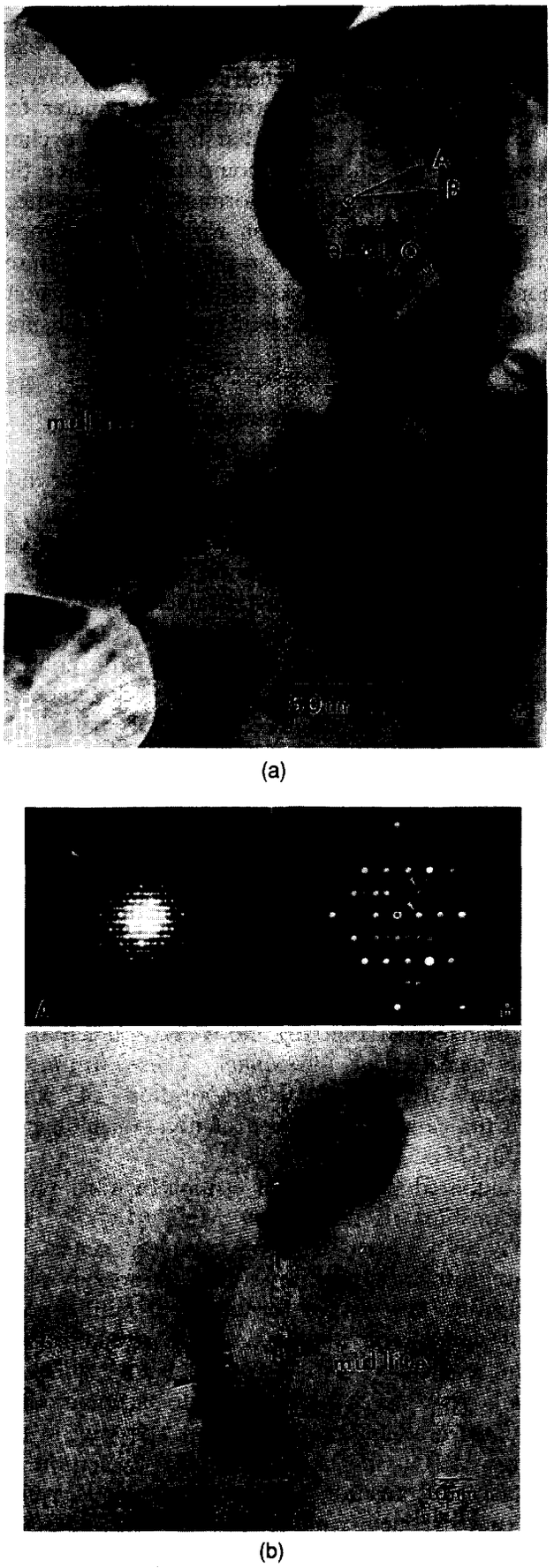

Fig. 14. (a) HREM image of mullite subgrains in [0 0 1] orientation, including an intragranular θ-Al_2O_3 particle. FOLZ and ZOLZ regions of a [$\bar{1}$ 3 1] zone axis pattern are shown in insets A and B in Fig. 14(b). (b) FOLZ and ZOLZ patterns obtained from θ-Al_2O_3 (top), [0 0 1] HREM image of mullite, exhibiting small intragranular precipitates with plannar defects, indicated by arrows (bottom).

(3) The formation of metastable transition polymorphs may also be controlled via the critical free energy for heterogeneous nucleation of alumina polymorphs. As emphasized by Ref. 38, the critical energy threshold is by definition lower for a transition alumina polymorph than for the thermodynamically stable phase corundum.

The frequent observation of transition alumina phases in plasma-sprayed alumina reported in the literature[7,21,22,38] and in mullite plasma layers, as observed during this research, can be rationalized in terms of Ostwald's step rule[39] which emphasizes the significance of the nucleation energy for crystallization of polymorphic systems. Such systems do not spontaneously form the most stable precipitation product, but rather pass sequentially through several intermediate stages with higher energies, before eventually the stable configuration with the lowest free energy is obtained.

The majority of mullite core grains investigated were homogeneous single phase 2/1-material. Reciprocal (h 0 l) lattice sections of mullite core grains (Fig. 15) yield the typical diffuse superstructure pattern[12,13] centred at a^*~1/3 and 2/3 and c^*~1/2, indicating that the distribution of oxygen vacancies on O(C) sites in the structure of as-sprayed mullite was not affected by the constraints of rapid solidification. However, some core grains were detected that contained nanoscale twin lamellae parallel to (0 0 1) planes. The twinned structure of such a core grain is displayed at high magnification in Fig. 16, after tilting the crystal into a [0 1 0] zone axis orientation so that the twin planes are edge-on. The corresponding diffraction pattern (see inset) is basically that of Fig. 15, superimposed with the effects of twinning

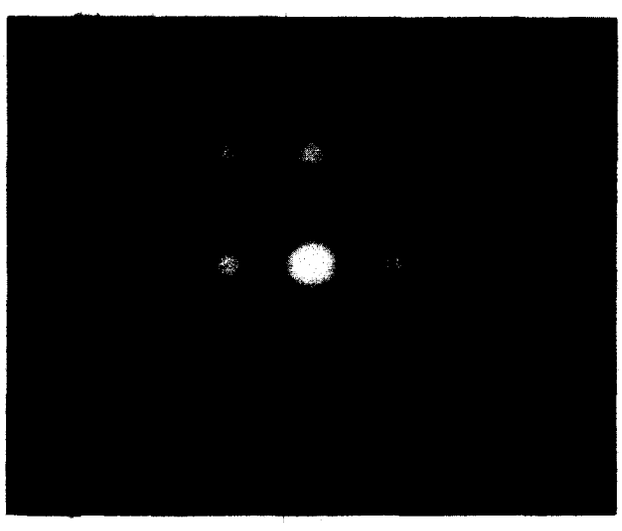

Fig. 15. ($h0l$) reciprocal lattice section of as-sprayed 2/1-mullite, displaying sharp and diffuse reflections as well as diffuse streaks in an a^*/c^* plot. The diffraction pattern was obtained from the mullite core grain shown in the inset of Fig. 4.

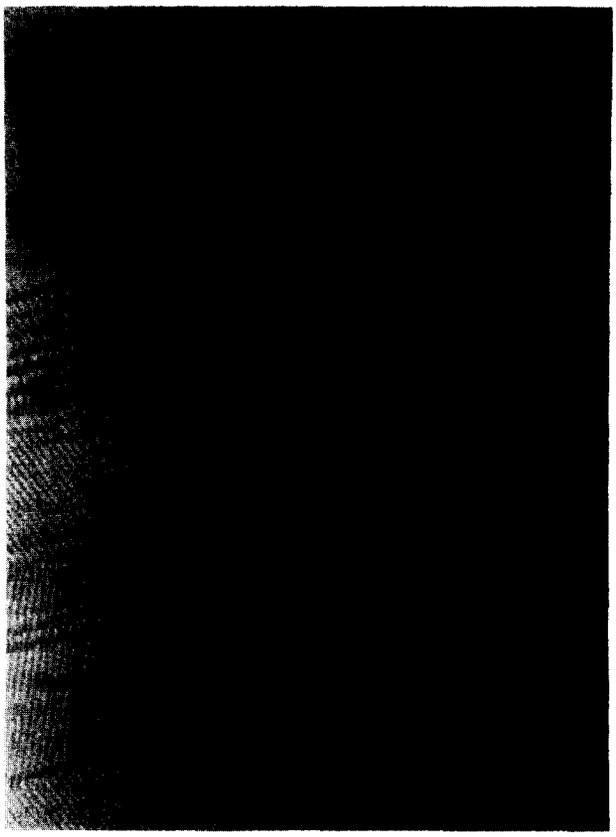

Fig. 16. Twin lamellae of as-sprayed mullite core grain, tilted into a [0 1 0] orientation (see corresponding SAD pattern inserted). The (0 0 1) twin boundaries are imaged edge-on.

on (0 0 1), as well as double diffraction as discussed in Ref. 33.

With ~79 wt% as determined via small-probe microanalysis (EDS), the Al_2O_3 content of the twinned mullite grain was considerably higher than the ~75 wt% Al_2O_3 for the untwinned species, determined by the same method. This finding is in fair agreement with the solid solution range-derived for melt-cooled mullites.[33] The Al_2O_3-rich end member, exceeding ~80 wt% Al_2O_3, incorporates the same twin structure as observed in the present study, while the 83 wt% Al_2O_3 batch exhibits exsolved αAl_2O_3 precipitates in a twin mullite matrix, indicating that the 83 wt% composition is the nominal mullite solid solution end member under normal conditions. It is believed that the formation of twinned Al-rich mullite core grains is controlled by the purity of the starting material and does not represent an intrinsic effect unique to the plasma-spraying process.

3.3 Nanoscale defect structure of as-sprayed spinel and mullite subgrains from impingement zones

The high quenching rates during deposition of thermally sprayed materials can introduce a variety of structural defects to the in-plane microstructure, which have been well explored for metallic systems in the literature.[7]

With the exception of the occasional twinned Al-rich mullites, (see Section 3.2), the core grains and the peripherical chill-zones in spinel and mullite are basically defect-free. If any structural defects are accumulated in the in-plane microstructure, they are clearly related to the impingement zone (see Section 3.1). The microstructurally irregular impingement zone provides a convenient sink for the relief of thermomechanical strains generated from the core and the chill-zone grains of the deposits. The strain energy released into the impingement zone not only gives rise to the formation of the typical subgrain structure dominated by small-angle grain boundaries (Figs 3 and 8), but also introduces intergranular cracks. Given a subsequent annealing treatment at high temperatures, substantial recrystallization of the impingement zone is expected to take place.

A more detailed TEM inspection shows that the subgrains from the spinel impingement zone contain characteristic structural defects such as point defects and stacking faults. For reasons related to the intrinsic differences in crystal structure between spinel and mullite, these defects are either less pronounced or completely absent in the analogous mullite microstructure:

(i) Spinel subgrains contained a significant level of point defects. Agglomeration of point defects resulted in formation of dislocation loops which were imaged in dark-field (Fig. 17). Smaller loops or point defect clusters appeared as white dots. No extra effort was undertaken in this study to discriminate between the different natures (vacancy versus interstitial type) of the loops. The thermal history of the spinel deposits investigated, however, strongly suggests that they resulted from agglomeration of thermal vacancies during the quench.

(ii) The subgrain boundaries in plasma-sprayed spinel layers acted as possible sinks for agglomeration of point defects, which eventually lead to the formation of the grain boundary precipitates discussed in Section 3.1.

(iii) The spinel subgrains contained planar faults lying on low-index planes, similar to those reported from Verneuil-grown spinel single crystals[40] and other spinel materials.[41] Depending on the local specimen thickness and the extinction distances of the reflections involved, these faults show typical α-fringe contrast when being studied under different imaging conditions.[42] In addition to straight fault segments, wavy faults associated with domain-like structures were observed in the spinel subgrains (Fig. 18). Although their characteristic appearance is similar to anti-phase boundaries (APB) in ordered f.c.c. alloys,[28] they are stacking faults because the corresponding SAD pattern did not reveal sharp superlattice reflections. This is different from most ordered crystal structures,[43,44] where strong APB fringe contrast is observed only for superlattice reflection, leaving no or only faint residual contrast for fundamental reflection images.

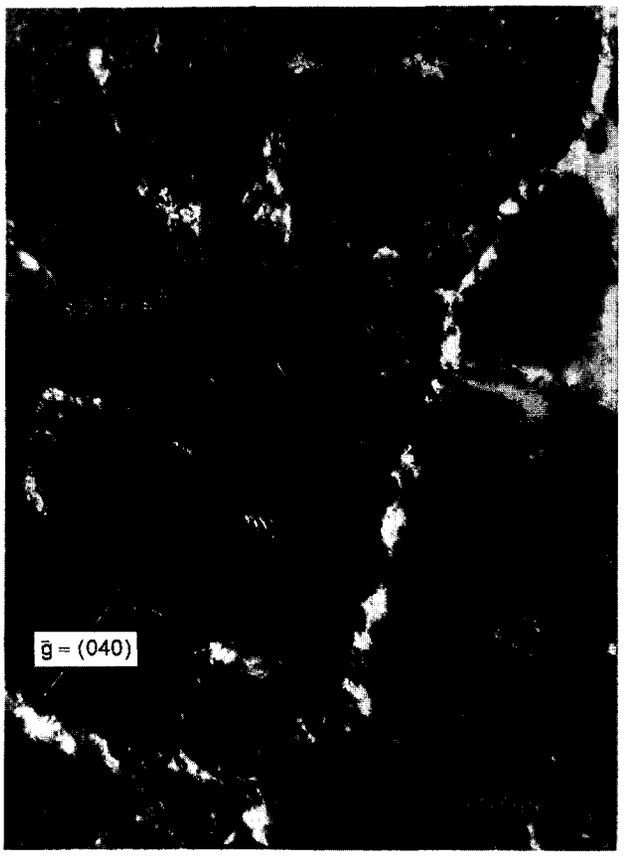

Fig. 17. Dark-field image from spinel subgrain taken with $\vec{g}$ = (0 4 0). Beam direction is parallel [1 0 3]. Small dislocation loops are indicated by arrows. The white band extending through the micrograph represents the trace of a subgrain boundary.

Moreover, the faults in plasma-sprayed spinel are arranged in an irregular, non-periodic

Fig. 18. Wavy faults in spinel subgrain (TEM BF). Beam direction is parallel to [3 1 $\bar{1}\bar{0}$].

pattern with a rather low density. Instead of generating a sharp, well-defined super-reflection, the low fault density in combination with their non-periodic arrangement give rise to weak diffuse streaks in reciprocal space only. The size of the streaks (~0·01 nm^{-1}) is given by the reciprocal value of the average fault-to-fault distance (see Fig. 18) which is 100 nm at the most. This is a much larger scale compared to ordered alloys such as CuAuII, where the APBs are regularly spaced with a period of ~0·2 nm.[43] The lattice spacing of the *g*(*hkl*) vectors controlling contrast in Fig. 18 is ~0·25 nm, resulting in a spot-to-spot distance of 4 nm^{-1} in the SAD pattern. Relative to this distance, the streaks resulting from the faults in spinel are less than 1% apart, leaving little margin to separate them clearly from the main Bragg spots.

Figures 19 and 20 demonstrate the effect of the faults by direct imaging of an appropriate set of spinel lattice planes. First, notice the rather limited distribution of curved faults (denoted by white arrowheads) in a spinel subgrain (Fig. 19). This micrograph also shows that the faults are pinned by the intragranular precipitates (indicated by black arrows) discussed in Section 3.1, or possibly by dislocations lying underneath the plane of the TEM foil (not shown). The precipitates act as obstacles for the mobility of fault segments during the coarsening process of the domain-like structure. The boxed area from a thin region of the specimen encompasses a typical fault/precipitate configuration and is shown at higher magnification in Fig. 20. The projection of the fault plane is almost edge-on in regions E and F where it appears quite narrow. In region D, it is inclined to the foil. The specimen was tilted to a [0 *k l*] orientation thus revealing {2 0 0} lattice fringes which extend across the whole area displayed in Fig. 20.

A close examination of the fringes in region E revealed that they are discontinuous across the trace of the fault plane: two stacks of {2 0 0} fringes (indicated by the black boxes marked 1 and 2) were selected from both sides of the fault, processed via digital image analysis and reassembled in the inset. When looking along the boundary between stacks 1 and 2 (see inset), the displacement of the {2 0 0} fringes by $a_O/2$ becomes obvious.

No systematic investigation of possible fault vectors in spinel has been conducted in this study. Although Fig. 19 provides the displacement of {2 0 0} planes in projection only, the situation displayed is consistent with displacement vectors of the type $a/2 \langle h\ 0\ 0 \rangle$ or $a/2 \langle 1\ 1\ 0 \rangle$ common to

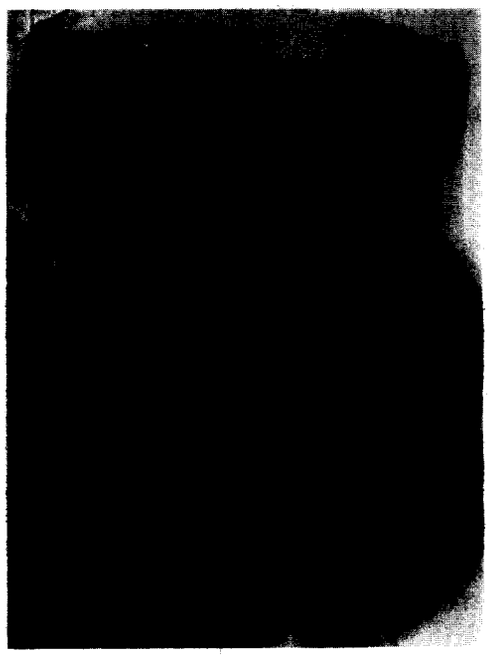

Fig. 19. Wavy stacking faults (indicated by white arrowheads) in spinel subgrain, pinned by low-angle tilt boundary (centre of micrograph) and intragranular precipipates (see black arrowheads). Beam direction is parallel [0 $\bar{5}$ 1]. Thickness fringes and bend contours are also visible due to buckling of the thin foil. For higher magnification of boxed region see Fig. 20.

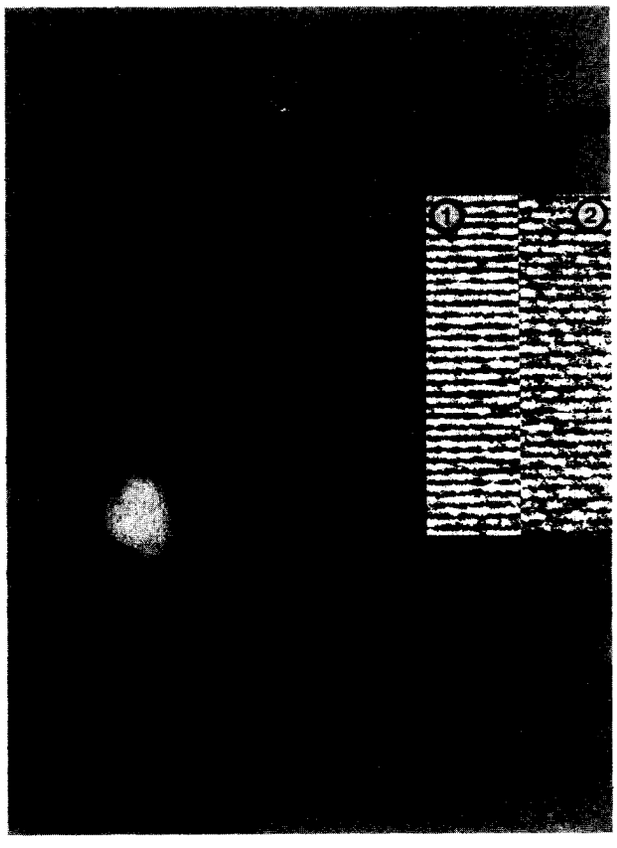

Fig. 20. Spinel {2 0 0} lattice fringes from a [0 $\bar{5}$ 1] orientation, showing the displacement of $a_O/2$ across a wavy fault in a subgrain (detail from Fig. 19). Two sets of {2 0 0} fringes (indicated by black boxes marked 1 and 2) were selected from both sides of the fault in region E, processed by digital image analysis and reassembled in the inset: the $a_O/2$ displacement becomes obvious along the boundary between stacks 1 and 2.

spinel,[40] depending on whether or not the displacement vector is confined to (0 $\bar{5}$ 1), the plane of presentation in Fig. 19. As discussed in Ref. 40, stacking faults in spinel have a preference for {1 0 0} followed by {1 1 0} and other low-index planes. It is the relatively isotropic stacking fault energy associated with low-index planes in spinel which gives rise to the formation of wavy rather than straight faults. The faults are considered as typical growth defects during lateral spread of the impingement zone.

4 Conclusions

The in-plane microstructure derived in the present TEM study illustrates the lateral growth pattern for the very first layers of plasma-sprayed Al_2O_3-rich ceramic feedstock materials. This interpretation relies on several assumptions, such as constant conditions during ultrasonic transport and deposition and negligible heat flow from the layer to the substrate due to rather poor adhesion. From these studies, the following conclusions can be drawn:

(1) Despite the rather chaotic impression the in-plane microstructure gives at first glance, the underlying growth pattern appears to be remarkably similar and straightforward for both spinel and mullite. It consists of a characteristic sequence starting from a large spherical defect-free core grain (region I) that acts as the nucleation site for a peripherical chill-zone (region II) exhibiting columnar to dendritic grain morphologies. During build-up of the layer, interference of different chill-zones leads to the formation of an impingement zone (region III). Due to the combined effects of the columnar grain morphology and the associated interlamellar porosity in the chill-zones as well as the microcracks in the impingement zones, the in-plane microstructure provides sufficient weak zones to accommodate residual stresses due to thermal expansion mismatch and/or thermal cycling.

(2) The occurrence of metastable submicrometre-sized transition alumina polymorphs in the mullite layer is related to the slow nucleation kinetics of stable constituents in the Al_2O_3–SiO_2 binary and may be rationalized in terms of Ostwald's step rule. The occasional formation of a twinned mullite species which is more Al_2O_3-rich compared to the average 2/1-mullite is most likely to be related to the purity of the feedstock material. The diffuse super-reflection pattern as derived from a^*c^* reciprocal lattice sections indicated that the structural short- and long-range order of as-sprayed mullite are left unaffected by the constraints of rapid solidification.

(3) While the core grains along with the surrounding chill-zones indicate the effects of thermal gradients during the early stages of deposition, the subgrain structure and the microcracks of the impingement zone reflect the relief of thermomechanical strains which have accumulated during lateral growth of the layer. The mosaic-like subgrain structure clearly reflects the thermally induced defect arrangement on growing grain impingement which is effective during solidification. Particularly in spinel, the impingement zone acts as the major sink for structural defects. This is documented by the agglomeration of point defects to form dislocation loops in the subgrains, the formation of grain boundary precipitates and the occurrence of often wavy stacking faults. Subsequent annealing treatments may favour recrystallization in the impingement zones associated with considerable grain growth.

Acknowledgements

It is a pleasure to acknowledge the stimulating discussions with G. Welsch, Case Western Reserve University, Cleveland, OH, USA and Ray Carpenter, Arizona State University, Tempe, AZ, USA (who also provided a critical review of the draft). This research was partially funded by a grant from the Deutsche Forschungsgemeinschaft (DFG), Bonn, Germany which is gratefully appreciated.

References

1. Harmsworth, P. D. & Stevens, R., Microstructure of zirconia–yttria plasma-sprayed thermal barrier coatings. *J. Mater. Sci.*, **27** (1992) 616–24.
2. Adam, P. & Johner G., Thermal barrier coatings (TBC) in aircraft engines. Status and lines of development. In *Advanced Materials Research and Developments For Transport. Ceramic Coatings For Heat Engines*, eds I. Kvernes, W. J. G. Bunk and I. G. Wurm. Les Editions de Physique, Les Ulis, 1985, pp. 265–87.
3. LeLait, L., Alpérine, S., Diot, C. & Mévrel, M., Thermal barrier coatings: microstructural investigation after annealing. *Mater. Sci. Eng.*, **A121** (1989) 475–82.
4. Kuroda, K., Hanagiri, S., Suginoshita, M., Taira, H., Tamura, S., Saka, H. & Imura, T., Microstructural characterization of plasma-sprayed oxide ceramics. *ISIJ Int.*, **29** (1989) 234–9.
5. Wilms, V. & Herman, H., Plasma spraying of Al_2O_3 and Al_2O_3–Y_2O_3. *Thin Solid Films*, **39** (1976) 251–62.
6. Wilms, V. H. S.,The microstructure of plasma sprayed ceramic coatings. PhD thesis, State University of New York, Stony Brook, NY, 1978.

7. Safai, S. & Herman, H., Plasma-sprayed materials. In *Treatise on Materials Science and Technology*, ed. H. Herman, Vol. 20. Academic Press, New York, 1981, pp 183–214.
8. Wang, H. G., Zhu, Y. M. & Herman, H., Structure of plasma-sprayed oxides in the $MgO–Al_2O_3–SiO_2$ system *J. Mater. Sci.*, **24** (1989) 4414–8.
9. Wang H. G. & Herman, H., Structure and properties of plasma-sprayed spinel. *Am. Ceram. Soc. Bull.*, **68** (1989) 97–102.
10. Gruetzner, H. & Weiss, H., Development of ceramic plasma-sprayed coatings against slag attack for the steel industry. In *Adv. Thermal Spraying: Proc. 11th Int. Thermal Spraying Conf.* Pergamon, New York, 1986, pp 349–57.
11. Cameron, W. E., Mullite: a substituted alumina. *Am. Mineral.*, **62** (1977) 747–55.
12. Guse, W. & Saalfeld, H., Das diffuse Beugungsbild von Mullit, 2 Al_2O_3·SiO_2. *Z. Krist.*, **143** (1976) 177–87
13. Saalfeld, H., The domain structure of 2:1 mullite (2 Al_2O_3·SiO_2). *N. Jb. Miner. Abh.*, **134** (1979) 305–16
14. Schneider, H. & Eberhard, E., Thermal expansion of mullite, *J. Am. Ceram. Soc.*, **73** (1990) 2073–6.
15. Aksay, I. A., Dabbs, D. M. & Sarikaya, M., Mullite for structural., electronic and optical applications *J. Am. Ceram. Soc.*, **74** (1991) 2358–68.
16. Butt, D. P., Mecholsky Jr, J. J., van Rodde, M. & Price, J. R., Effects of plasma sprayed ceramic coatings on the strength distribution of silicon carbide materials *J. Am. Ceram. Soc.*, **73** (1990) 2690–6.
17. Henne, R. & Weber, W., Progress in the development of high-temperature oxidation-preventing coatings for molybdenum by application of the low-pressure-plasma-spraying technique. *High Temp. High Pressures*, **18** (1986) 223–32.
18. Disam, J., Sickinger, A. & Wilms,V., The effect of the chamber and spraying parameters of the LPPS method on the structure of mullite coatings, *Conf. on Thermal Research and Applications*, Long Beach, CA, May 1990.
19. Levin, E. M., McMurdie, H. F. & Reser, M. K. (eds), *Phase Diagrams For Ceramists*, 3rd edn, The American Ceramic Society, Columbus, OH, 1974.
20. Doukhan, N., Doukhan, J. C. & Escaig, B., TEM study of high temperature precipitation in $(Al_2O_3)_n$ MgO spinels *Mater. Res. Bull.*, **11** (1976) 125–34.
21. McPherson, R., Formation of metastable phases in flame- and plasma-prepared alumina. *J. Mater. Sci.*, **8** (1973) 851–8.
22. Dauger, A., Fargeot, D. & Laval, J. P., Metastable phases of alumina. In *Mater. Res. Soc. Symp. Proc. Vol. 21*. The Materials Research Society, Pittsburgh, PA, 1984.
23. Chuanxian, D., Zatorski, R. A. & Herman, H., Oxide powders for plasma spraying — the relationship between powder characteristics and coating properties. *Thin Solid Films*, **118** (1984) 467–75.
24. McPherson, R. & Shafer, B. V., Interlamellar contact within plasma-sprayed coatings. *Thin Solid Films*, **97** (1982) 201–4.
25. Shi, K. S., Quian, Z. Y. & Zhuang, M. S., Microstructure and properties of sprayed ceramic coatings. *J. Am. Ceram. Soc.*, **71** (1988) 924–9.
26. Lutz, E. H., Microstructure and properties of plasma ceramics. *J. Am. Ceram. Soc.*, **77** (1994) 1274–80.
27. Hsueh, C. H., Some considerations of determination of residual stresses and Young's moduli in ceramic coatings. *J. Am. Ceram. Soc.*, **74** (1991) 1646–9.
28. Porter, D. A. & Easterling, K. E., *Phase Transformations in Metals and Alloys*. Van Nostrand Reinhold, New York, 1981.
29. Troeger, W. E., Optische Bestimmung der gesteinsbildenden Minerale, Teil 2. In *E. Schweizerbart'sche Verlagsbuchhandlung*. Naegele & Obermiller, Stuttgart, 1971.
30. Michel, D., Mazerolles, L. & Portier, R., Directional solidification in the alumina–silica system: microstructures and interfaces. In *Mullite and Mullite Matrix Composites*, eds S. Somiya, R. F. Davis and J. A. Pask. The American Ceramic Society, Westerville, OH, 1990.
31. Powell-Dogan, C. A. & Heuer, A. H., Microstructure of 96% alumina ceramics: I. Characterization of the as-sintered materials. *J. Am. Ceram. Soc.*, **73** (1990) 3670–6.
32. Merk, N. & Thomas, G., Structure and composition characterization of submicronic mullite whiskers. *J. Mater. Res.*, **6** (1991) 825–34.
33. Kriven, W. M. & Pask, J. A., Solid solution range and microstructures of melt-grown mullite. *J. Am. Ceram. Soc.*, **66** (1983) 649–54.
34. Pask, J. A., Critical review of phase equilibria in the $Al_2O_3–SiO_2$ system. In *Ceramic Transactions Vol. 6: Mullite and Mullite Matrix Composites*, eds S. Somiya, R. F. Davis and J. A. Pask. The American Ceramic Society, Westerville, OH, 1990, pp. 1–13.
35. Wefers, K. & Misra, C., Oxides and hydroxides of aluminum, Alcoa Technical Papers No. 19, Aluminum Company of America, Pittsburgh, PA, 1987.
36. Wilson, S. J., Phase transformations and development of microstructure in boehmite-derived transition aluminas. *Br. Cer. Soc. Proc.*, **28** (1979) 281–94.
37. Morrissey, K. J., Czanderna, K. K., Merrill, R. P. & Carter, C. B., Transition alumina structures studied using HREM. *Ultramicroscopy*, **18** (1985) 379–86.
38. McPherson, R., On the formation of thermally sprayed alumina coatings. *J. Mater. Sci.*, **15** (1980) 3141–9.
39. Ostwald, W., Studien ueber die Bildung und Umwandlung fester Koerper 1. Abhandlung: Uebersaettigung und Ueberkaltung. *Z. Physik. Chemie*, **22** (1897) 289–330.
40. Lewis, M. H., Defects in spinel crystals grown by the Verneuil process. *Phil. Mag.*, **14** (1966) 1003–18.
41. Mitchell, T. E., Lagerloef, K. P. D. & Heuer, A. H., Dislocations in ceramics. In *Dislocations and Properties of Real Materials: Proc. 5th Anniversary of the Concept of Dislocation in Crystals*. The Institute of Metals, London, 1985.
42. Amelingckx, S. & van Landuyt, J., Contrast effects at planar interfaces. In *Electron Microscopy in Mineralogy*, ed. H. R. Wenk. Springer, Berlin, 1976, 68–112.
43. Glossop, A. B. & Pashley, D. W., The direct observation of abti-phase domain boundaries in ordered copper–gold (CuAu) alloy. *Proc. Roy. Soc.*, **A250** (1959) 132–46.
44. Hirsch, P., Howie, A., Nicholson, R. B., Pashley, D. W. & Whelan, M. J., *Electron Microscopy of Thin Crystals*. Robert E. Krieger Publishing Company, 1977.